Multi-axis Active Vibration Suppression for Wafer Transfer Systems

Jiajie Qiu[1†], Hongjin Kim[2†], Fangzhou Xia[1*], and Kamal Youcef-Toumi[1]

Abstract—Vibration suppression is critical in precision mechatronic systems for nanofabrication. For automated wafer handling in semiconductor plants, Overhead Hoist Transport (OHT) vehicles transport wafers carried in Front Opening Unified Pods (FOUPs); while the wafers are transported in a FOUP, semiconductor chips are at risk of damage by excited small particles due to mechanical vibration. Active suppression of the FOUP vibrations has been proposed to improve the production yield. However, there are two main challenges that make it a non-trivial problem. First, moving FOUPs carried by the OHT vehicles have no external anchoring point as a momentum source for control efforts. Second, no sensor attachment is permitted on mass-production FOUPs, which makes feedback control more challenging without measurement. Since the goal is to suppress the large FOUP acceleration peaks instead of eliminating all vibration, an inertia-based counterbalancing system is designed to address these challenges. To validate this idea, a custom testbed is designed for multi-axis vibration generation and suppression. A Disturbance Observer-Based Controller (DOBC) is developed and implemented on the hardware. During the experiment, 38 percent of the OHT hand unit vibration (and 42 percent of FOUP vibration) suppression is achieved in the OHT travel direction. Moreover, multi-axis FOUP-level acceleration-peak reduction is achieved to verify the effectiveness of the proposed method.

Index Terms—Motion Vibration Control, Identification and Estimation in Mechatronics, Control Application in Mechatronics, Disturbance Observer, Overhead Hoist Transport Vehicle

I. INTRODUCTION

In modern semiconductor fabrication plants, the Overhead Hoist Transport (OHT) system is widely used to transport 300 *mm* wafers between hundreds of processing steps. The wafers are stored in a Front Opening Unified Pod (FOUP) and the OHT vehicles carry FOUPs using OHT hand units. Due to the number of transportation required, it is important to keep the wafers intact during transportation. Among many wafer quality management factors, researchers of Samsung Electronics discovered that the vibration acceleration level of FOUPs is a critical factor since dust particles in FOUPs can be excited by the vibration and damage semiconductor products if they land on critical areas of the wafers [1–3]. As the semiconductor miniaturization technology advances, the current vibration reduction strategy of Samsung Electronics using passive damping materials does not achieve adequate performance. Therefore, active vibration control techniques are developed in this paper for further vibration level reduction.

[1] Massachusetts Institute of Technology Mechatronics Research Laboratory, 02139, Cambridge, MA, USA
[2] Samsung Electronics, email: hongjin7.kim@samsung.com
* Corresponding author: Fangzhou Xia, email: xiafz@mit.edu
† These authors contributed equally to this work.

Compared to classical vibration suppression tasks, there are two unique challenges with the FOUP system. First, there exist no external anchoring points to be used as a momentum source during transportation. This is in principle different from many large-scale static building or optical table applications where many different types of Tuned Mass Damper (TMD) systems are applied as a solution [4–8]. Compared to vehicle applications, suppression of the FOUP in-plane vibration levels along traveling and lateral directions also has more stringent requirements. Second, the acceleration level of the FOUP cannot be directly measured, which makes this control problem different from many other situations where direct state observation is possible [9, 10]. This is due to the current design restriction of the semiconductor fabrication plants, where no sensor attachments are permitted on mass-production FOUPs.

This research focuses on multi-axis vibration suppression. Previous work of the authors [11] succeeded in controlling the hand unit vibration displacement in the traveling axis (denoted as X-axis) when the disturbance is only applied in the same axis. However, the disturbance in the lateral axis (denoted as Y-axis) will also have an effect on the X-axis, and vice versa. This is because the hand unit is hung in the OHT vehicle via three hoist cables, as shown in Fig. 1. As a result, the original system and the testbed design (to be introduced in Section II) can cause motion coupling between the X and Y axis. Thus, the designed controller should not only be able to compensate for the disturbance affecting this axis but also resist all the dynamic effects from the orthogonal axis. Note that the twisting mode can in principle also be excited due to a small misalignment in the external force source on our testbed. However, this is not important in the practical operations of real systems and is therefore neglected.
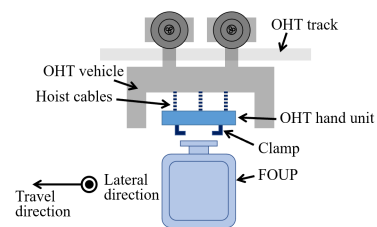

Fig. 1. Schematic of the OHT vehicle, hand unit, and FOUP interface.

The main contributions of this work include:
1) Design and implementation of a multi-axis vibration generation testbed and a multi-axis inertia-based vibration suppression hardware system. The system can generate and suppress vibrations for the OHT hand unit-FOUP system in both travel and lateral axes simultaneously.

2) Development of a multi-axis active vibration suppression controller on the OHT hand unit-level and passive vibration transmission reduction mechanism between the hand unit and the FOUP.
3) Reproducible system identification procedure of the disturbance observer design.
4) Simulation and experimental validation of the simultaneous multi-axis vibration controller on both OHT displacement and FOUP acceleration.

The paper is organized as follows. In Section II, the design of the multi-axis vibration generation testbed (to emulate the real OHT track system) and the controller hardware implementation are introduced. In Section III, a linear dynamic system model is developed. System identification techniques are applied to identify both the single-axis system and the multi-axis system where both vibration actuators are connected to the hand unit with stingers. Numerical transfer functions are fitted for controller design. In Section IV, a multi-axis controller is designed for active vibration suppression and implemented on the hardware. The performance results are presented to verify the controller. Section V discusses how to further improve the vibration control performance. Finally, the conclusions and future works are summarized in Section VI.

II. HARDWARE SYSTEM DESIGN

The hardware design of this work includes a multi-axis vibration generation testbed and an on-board inertia-based multi-axis vibration suppression system.

A. Vibration Generation Testbed Design

The multi-axis vibration generation testbed is designed based on the single-axis testbed [11], as shown in Fig. 2. In addition to the existing vibration generation voice coil actuator (VCA, VCAR0436-0250-00A; SUPT Motion) in the OHT travel direction (X-axis), another identical VCA is mounted in the OHT lateral direction (Y-axis).

Both vibration generation VCAs are connected to the hand unit with modal stingers (2155G12; The Modal Shop, Inc.). Stingers are stiff in the axial direction but flexible in the radial direction. They can transmit the actuator force with minimum disturbance to the alignment of the VCA coils and magnets.

The data acquisition system shown in Fig. 3 is also developed based on [11] but includes more modules. Two extra H-bridge motor driver modules (NI9505) are used to drive the vibration generation VCA and the vibration suppression VCA in the Y-axis. An extra digital-IO module (NI9402) is added to interface with the linear encoders to measure the displacement of the hand unit in the Y-axis and the position of the moving mass of the Y-axis vibration suppression VCA.

B. Vibration Suppression System Design

The multi-axis vibration suppression system extends the capability of the single-axis system developed previously [11]. Besides the existing vibration control VCA (VCAR0033-0224-00A; SUPT Motion) mounted in the OHT travel direction (X-axis), another identical vibration control VCA is mounted in the OHT lateral direction (Y-axis), as shown in Fig. 4. The maximum momentum that the inertia-based vibration
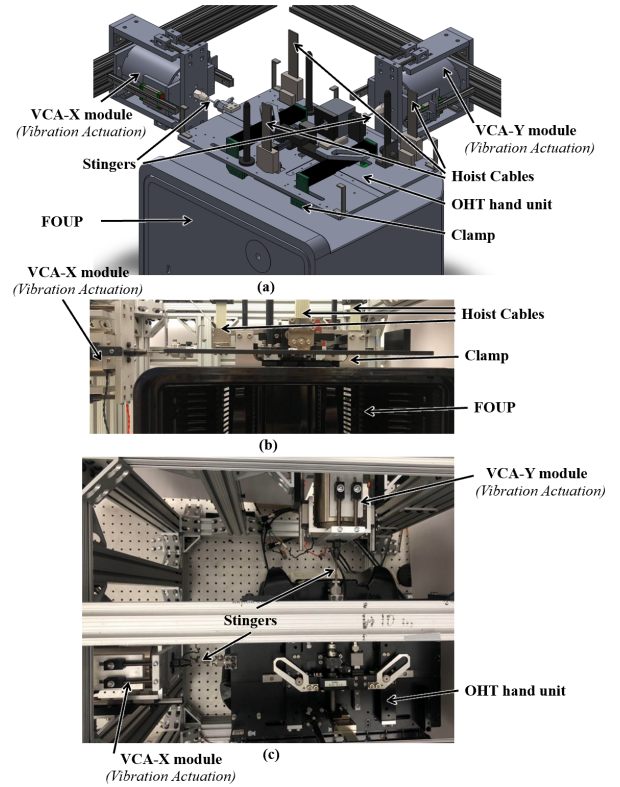

Fig. 2. (**a**) CAD of the vibration testbed and (**b**) front view of the assembled testbed. (**c**) top view of the assembled testbed.
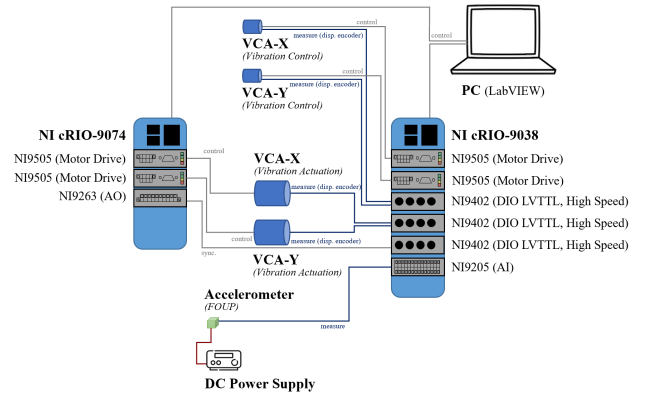

Fig. 3. Schematic of the mechatronic connection for the vibration generation testbed and the vibration suppression actuators.

suppression system can generate is limited due to the relatively small driven mass and short stroke of the VCAs. Collision between the moving mass (the VCA magnet mounted on linear bearings) and the base is possible, and must be avoided to prevent any additional disturbances to the system.

III. SYSTEM CHARACTERIZATION

Dynamic system modeling and identification are important for understanding the system's behavior and designing the controller. The system model is first linearized to a lumped parameter model, and the corresponding parametric transfer function is determined. Next, sinusoidal input frequency sweep
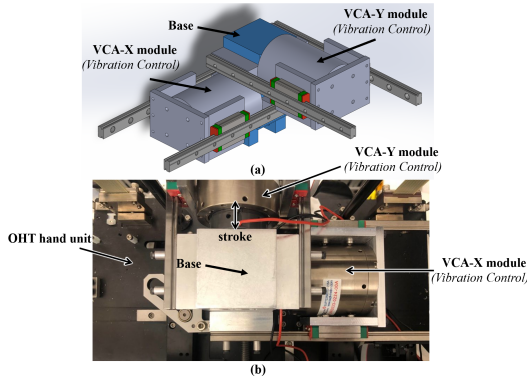
Fig. 4. (**a**) CAD of the vibration suppression actuator and (**b**) top view of the assembled vibration suppression system on the hand unit.

is implemented to obtain the magnitude and phase of the system at different frequencies. Finally, a numerical transfer function is fitted to the measurement based on the parametric equations. As the multi-axis system is more complicated, this work starts with identifying the single-axis dynamics, where the other axis vibration actuator is disconnected from the hand unit. Identification of the multi-axis system is performed when both axes are connected to the hand unit with stingers. As shown in Eq. (1), four transfer functions H_{xx}, H_{xy}, H_{yx}, and H_{yy} exist between two input forces F_x and F_y (our testbed simulates the disturbances of real systems with forces generated by VCAs) and the output displacement X and Y. With orthogonal axis, the main linear dynamics for control are H_{xx} and H_{yy}. Due to some limitations in our testbed design, the coupled H_{xy} and H_{yx} are highly nonlinear due to the twisting motion and thus are treated as additional disturbance sources during control.

$$\begin{bmatrix} X(s) \\ Y(s) \end{bmatrix} = \begin{bmatrix} H_{xx}(s) & H_{xy}(s) \\ H_{yx(s)} & H_{yy}(s) \end{bmatrix} \begin{bmatrix} F_x(s) \\ F_y(s) \end{bmatrix} \quad (1)$$

A. System Modeling

For modeling purposes, the system is simplified to a lumped parameter mass-spring-damper model in the mechanical domain. The testbed shown in Fig. 2 can be modeled as the linear system shown in Fig. 5. The small angle approximation is applied here to linearize the hoist cable connection between the hand unit and the testbed frame.
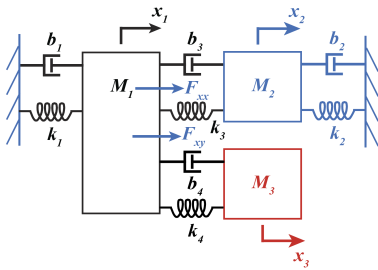

Fig. 5. A linear mass-spring-damper model of the connections between the testbed, the hand unit, and the FOUP. The testbed frame is denoted in blue, the hand unit is black, and the FOUP is red.

The variables in Fig. 5 are defined below:

- M_1: total mass of the actuation VCA and the hand unit
- k_1, b_1: equivalent spring and damper of the VCA-to-solid-ground connection
- M_2: mass of the testbed frame (a cantilever system)
- k_2, b_2: lumped spring and damper of the testbed frame
- k_3, b_3: equivalent spring and damper of the hoist cables connecting the hand unit and the frame
- M_3: mass of the FOUP
- k_4, b_4: equivalent spring and damper of the clamp between the hand unit and the FOUP
- F_{xx}, F_{xy}: the X-component of the forces from the X-axis and Y-axis disturbances

It is important to note that the vibration of the FOUP (M_3) is transferred from the OHT motion. As the OHT travels, the hand unit clamp modeled as a spring-damper system provides the force to generate the acceleration on the FOUP, which is only related to the relative displacement and velocity between the hand unit and the FOUP. In the actual implementation, no motion measurement data can be obtained from the FOUP due to design constraints. Therefore, this work focuses on feedback control of the hand unit displacement. If OHT hand unit vibration displacement is suppressed, the force transmitted to the FOUP will also be reduced. As a result, the FOUP vibration acceleration will be reduced, which can be verified by a sensor installed on the FOUP of the testbed.

B. System Identification

To control the displacement of the hand unit, the transfer function relating the disturbance force F_{xx} to the hand unit position x_1 is derived from Fig. 5 as shown in Eq. (2).

$$\frac{X_1(s)}{F_{xx}(s)} = \frac{BC}{ABC - (b_3 s + k_3)^2 - (b_4 s + k_4)^2} \quad (2)$$

where

$$\begin{cases} A = M_1 s^2 + (b_1 + b_3 + b_4)s + k_1 + k_3 + k_4 \\ B = M_2 s^2 + (b_2 + b_3)s + k_2 + k_3 \\ C = M_3 s^2 + b_4 s + k_4 \end{cases}$$

1) Single-axis System Identification: To identify the hand unit-FOUP system H_{xx} along the X-axis when the Y-axis vibration actuator is disconnected, a frequency sweep from 0.2 Hz to 15 Hz with 0.1 Hz interval is implemented. The Lock-in amplifier is used on the input force F_{xx} and the displacement output x to obtain the magnitude and phase of the system at each frequency and to filter out measurement noise. A numerical transfer function is fitted to the measurement based on the parametric expression in Eq. (2). Python package *SciPy* is used for the fitting. The logarithmic transfer function is fitted to the logarithmic magnitude measurement with the "Trust Region Reflective" method. The fitted model and the measurement results are plotted in Fig. 6.

As shown in Fig. 6, there are three resonant peaks at 3.2 Hz, 5.3 Hz, and 9 Hz, and two anti-resonant peaks at 3.6 Hz and 5.7 Hz. The result matches the linear model in Eq. (2), where there are two pairs of conjugated complex zeros on the numerator and three pairs of conjugated complex poles on the denominator. The fitting toolbox tends to ignore the first resonant and anti-resonant peaks to capture the main
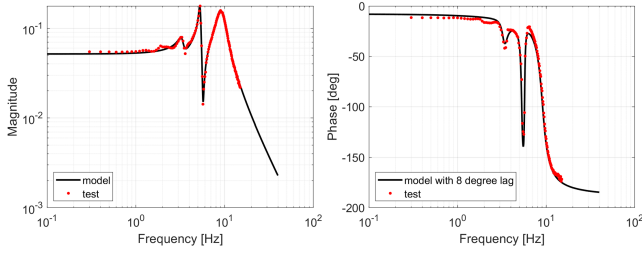
Fig. 6. Bode plot of the single-X-axis system between the input force and the hand unit displacement. The black curve is the linear model, and the red dots are the measurements. A lag of 8° is added to the linear model phase to fit with the measurement better.
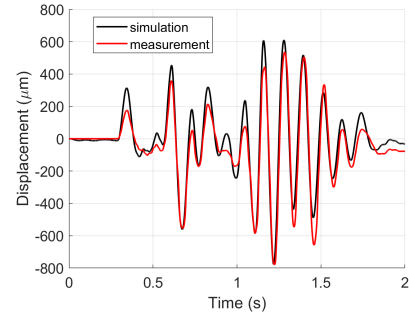

Fig. 7. Comparison of the measured displacement and the Simulink simulated result. The black curve is the simulation of the transfer function Eq. (3), and the red curve is the measurements from the hardware.

dynamics that appear after 4 Hz to minimize error. However, our previous work [11] shows that the system without the FOUP has resonant and anti-resonant peaks at 4 Hz and 4.2 Hz. With the FOUP as an extra mass added to the system, it is expected that the previous resonant and anti-resonant peaks will shift slightly to a lower frequency. Thus, the magnitude features at 3.2 Hz and 3.6 Hz are the expected resonant and anti-resonant peaks and should not be ignored.

To capture this feature, all the complex conjugate poles and zeros in the parametric model are written in the form of $(s^2 + 2as + \omega_P^2 + 2a^2)$. a and ω_P are the parameters to be fitted, where a is the product of the damping ratio ζ and natural frequency ω_n, and ω_P is the resonant (or anti-resonant) frequency. Upper and lower boundaries are assigned to the parameters for reasonable fitting results. A boundary of ± 2 Hz around the measured peak frequency is added to the ω_P. The boundary of a is set to be $[0, \infty]$. The fitted numerical transfer function is shown in Eq. (3).

$$\frac{X(s)}{F_{xx}(s)} = \frac{Gain_1(s^2 + 3.69s + 465.1)(s^2 + 1.3s + 1289)}{(s^2 + 3.2s + 438)(s^2 + 2s + 1109)(s^2 + 14s + 3253)}$$
(3)

As shown in Fig. 6, the measurement has a certain phase lag (about 8°) compared to the fitted linear model. This is caused by the friction in the linear bearing used for the VCA coil alignment. After lubricating the linear bearing, the phase lag is reduced but still exists.

The fitted linear model is verified by comparing the simulation and measurements of the displacement x with a pre-designed input force F_{xx}. The model is simulated in Simulink with the continuous transfer function block. Both the simulation and measurement are plotted in Fig. 7.

As shown in Fig. 7, the peaks of the measurement always appear after the simulation, which matches the observed phase lag. Despite the unmodeled nonlinearities, the simulation captures the main trend of displacement for controller design.

2) Multi-axis System Identification: An identical procedure is also applied to the multi-axis system. In this system, both X-axis and Y-axis vibration actuators are connected to the hand unit with stingers. In this work, the transfer function between the X(or Y)-axis input force F_x (or F_y) and the X(or Y)-axis displacement x (or y) are determined. The following shows the procedure for determining the transfer function between F_x and x. Frequency sweep using a similar technique is applied (from

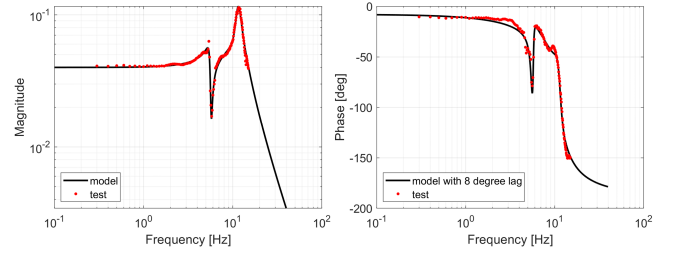0.2 Hz to 15 Hz with 0.1 Hz interval) to generate the Bode plot, as shown in Fig. 8.

Fig. 8. Bode plot of the dynamics between F_x and X. The black curve is the linear model, and the red dots are the measurements. A lag of 8° is added to the linear model phase to fit with the measurement better.

As shown in Fig. 8, one resonant peak and one anti-resonant peak disappear compared to the single-X-axis system. This is because, when the Y-axis vibration actuator is connected, the Y-axis stinger and VCA restrict the movement of the hand unit as a spring and damper to change k_3 and b_3, which damp the corresponding resonance peak. The fitted transfer function is plotted in Fig. 8 and shown in Eq. (4).

$$\frac{X(s)}{F_x(s)} = \frac{Gain_2(s^2 + 1.54s + 1305)(s^2 + 19.2s + 4633)}{(s^2 + 3.5s + 1219)(s^2 + 11s + 5197)(s^2 + 45s + 4766)}$$
(4)

The fitted linear model is verified by comparing the simulation and measurement results of the displacement x with a pre-designed input force F_x as shown in Fig. 9.
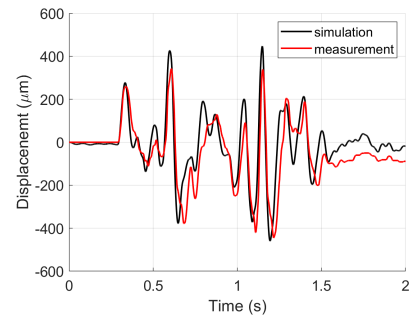

Fig. 9. Comparison of the measured displacement and the simulated result. The black curve is the Simulink simulation of the transfer function Eq. (4), and the red curve is the measurement from the hardware.

The linear model captures the main characteristic of the real system, and can be used for the controller design of the multi-axis system.

IV. VIBRATION SUPPRESSION CONTROLLER DESIGN

In this section, a Disturbance Observer-Based Controller (DOBC) is designed for the multi-axis vibration control task. A DOBC is first designed based on the identified single-axis system and tested on the hardware. The result proves that the DOBC can observe the main feature of the disturbance in the designed direction, and the hand unit displacement control enables the FOUP vibration suppression. Next, two DOBCs are designed for the X and Y axes based on the identified multi-axis system and tested on the hardware. The result shows that the DOBC can suppress the vibration in the coupled multi-axis system when the disturbances are applied simultaneously.

A. Single-axis System Control

The design of the controller for the single-axis system is shown in this section. A disturbance observer is first designed based on the transfer function between the input force in each direction and the hand unit displacement. A PI controller is added to compensate for the model error and other disturbance sources. Another PI controller is added to control the controller actuator moving mass position to avoid the collision between the moving mass and the base (a design concern mentioned in Section II-B). To design the disturbance observer for the single-X-axis system, the transfer function between the input disturbance F_x and the hand unit X-axis displacement x is simplified and inverted. Two low-pass filters are added to avoid the instability caused by having more zeros than poles and by differentiating the measurement. The transfer function of the disturbance observer is shown in Eq. (5).

$$\frac{\hat{F}_x(s)}{X(s)} = \frac{\text{Gain}_3(s^2+2.3s+1109)(s^2+14.4s+3234)}{(s^2+1.19s+1293)(s+80)^2} \quad (5)$$

The disturbance observer transfer function is discretized in Matlab with the *c2d* command "Zero-Order Hold" method at a sampling frequency of 10 kHz, which is the hardware controller loop frequency on FPGA. After rearranging the z-domain transfer function using $x[k]z^{-1} = x[k-1]$, the discretized disturbance observer can be implemented in Eq. (6).

$$
\begin{aligned}
F[k] = {} & 3.983931656F[k-1] - 5.9518734899F[k-2] \\
& + 3.9519517973F[k-3] - 0.9840099642F[k-4] \\
& + \text{Gain}_4(0.715853206x[k] - 2.8621849758x[k-1] \\
& + 4.2914668615x[k-2] - 2.8597916022x[k-3] \\
& + 0.7146565108x[k-4])
\end{aligned} \quad (6)
$$

In practical implementation, high precision coefficients should be utilized to avoid unstable estimation caused by errors induced by the high sampling rate and the high-order observer transfer function. The Fixed-point type in LabVIEW is set to a precision of 10^{-13}, which is enough for the designed disturbance observer.
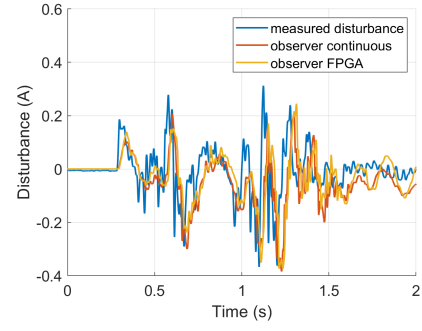

Fig. 10. Comparison between the input disturbance (blue curve), observed disturbance in Simulink (red curve), and the observed disturbance on hardware FPGA (yellow curve).

The designed disturbance observer is evaluated first in Simulink simulation and later verified on hardware implemented in LabVIEW FPGA. With the same displacement input, the observed disturbance are plotted in Fig. 10.

As shown in Fig. 10, the FPGA calculated disturbance has some discrepancies compared to the Simulink simulation. Despite some errors and phase lag due to the simplification of the model and the low-pass filter, the observer captured the main dynamics of the input disturbance. Note that the 64-bit fixed-point numbers on the FPGA can also accumulate a certain level of error during calculations.

The overall controller block diagram is shown in Fig. 11. A PI controller for the hand unit position control is added for compensation of unobserved disturbances (e.g. axes coupling). Another PI controller for the counterbalancing mass is added to gradually move the inertia to its center position to prepare for the next disturbance peak. $G_{\text{HU}}(s)$ and $G_{\text{MM}}(s)$ are the plant of the single-X-axis system transfer function in Eq. (3), and the transfer function between the input current and the position of the moving mass. $H_{\text{HU}}(s)$ and $H_{\text{MM}}(s)$ are the measurement block for the hand unit displacement and the moving mass displacement. r_{HU} and r_{MM} are the reference values for the hand unit and moving mass displacement, which are both set to be 0. The $\frac{1}{\bar{G}_{\text{HU}(s)}}$ and the filter block represent the disturbance observer to estimate the disturbance force F_{D}. x_{D} is the displacement due to all the unmodeled disturbances from the coupled dynamics between axes and is added to influence the hand unit displacement x_{HU}.
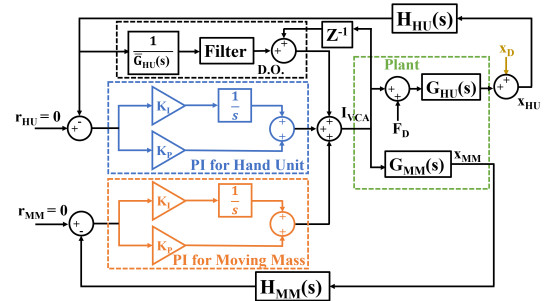

Fig. 11. Overall controller block diagram.

Using controller parameters from the previous work [11], the performance is shown in Fig. 12.
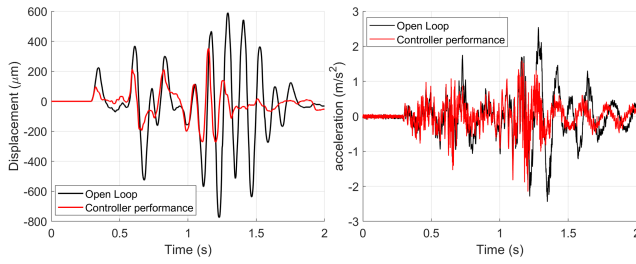
Fig. 12. Left: the hand unit displacement in the X-axis with a designed disturbance input in open loop (black curve) and in controlled closed loop (red curve); Right: the FOUP acceleration in the X-axis in open loop (black curve) and in controlled closed loop (red curve).

As shown in Fig. 12, the maximum hand unit displacement peak is suppressed from 773.75 μm to 352.5 μm, and the maximum FOUP acceleration peak is suppressed from 2.55 m/s^2 to 2.15 m/s^2. The hand unit displacement control also suppresses the acceleration of the FOUP. It confirms that the modeling of the clamp to a parallel spring-damper system is correct, and that the suppression of the hand unit displacement will reduce the FOUP vibration acceleration.

B. Multi-axis System Control

The X-axis controller design for the multi-axis system is presented in this section. The Y-axis controller design follows the same procedure, thus is omitted here to avoid redundancy. The disturbance observer is designed based on the transfer function Eq. (4) between the X-axis disturbance F_x and the X-axis hand unit displacement x of the multi-axis system. All the influences from the Y-axis are treated as minor disturbance sources and should be suppressed by the parallel PI controller.
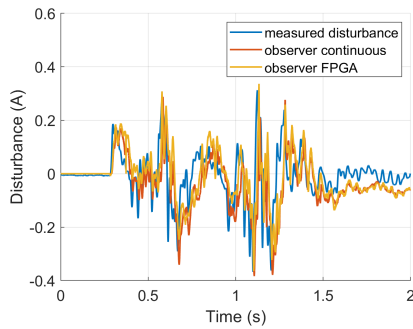

Fig. 13. Comparison between the input disturbance (blue curve), observed disturbance in Simulink (red curve), and the observed disturbance on hardware FPGA (yellow curve).

The disturbance observer design for the multi-axis system follows the same procedure mentioned in Section IV-A. The designed disturbance observer is tested in both Simulink and on FPGA hardware, as shown in Fig. 13. The observer captures the main features and peaks of the disturbance, despite the errors and phase lag due to the number rounding, simplification of the model, and the low-pass filter.

With the same double PI in Section IV-A added parallel to the controller, the controller is first verified when both X-axis and Y-axis vibration actuators are connected to the hand unit with stingers, but only the X-axis vibration actuator is applying a disturbance on the hand unit. The performance is shown in Fig. 14, where the maximum hand unit displacement peak is suppressed from 445 μm to 275 μm, and the maximum FOUP acceleration peak is suppressed from 4.70 m/s^2 to 4.09 m/s^2.
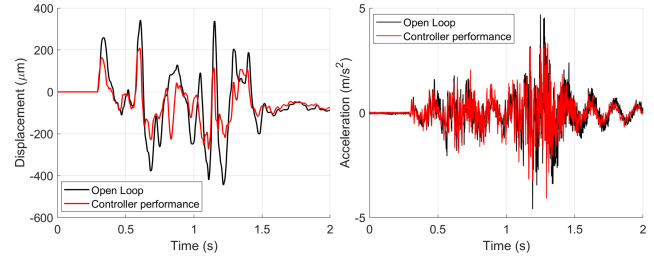

Fig. 14. Left: the hand unit displacement in X-axis with a designed disturbance input in open loop (black curve) and in controlled closed loop (red curve); Right: the FOUP acceleration in X-axis in open loop (black curve) and in controlled closed loop (red curve)

After designing the Y-axis controller using the same procedure, multi-axis active vibration suppression is verified by turning on the vibration generation and suppression along both axes simultaneously. The controller performance is shown in Fig. 15. Along the X-axis, the maximum hand unit displacement peak is suppressed from 816.25 μm to 506.25 μm, and the maximum FOUP acceleration peak is suppressed from 6.11 m/s^2 to 3.53 m/s^2. In the Y-axis, the maximum hand unit displacement peak is suppressed from 736.25 μm to 538.75 μm, and the maximum FOUP acceleration peak is suppressed from 3.85 m/s^2 to 2.59 m/s^2.
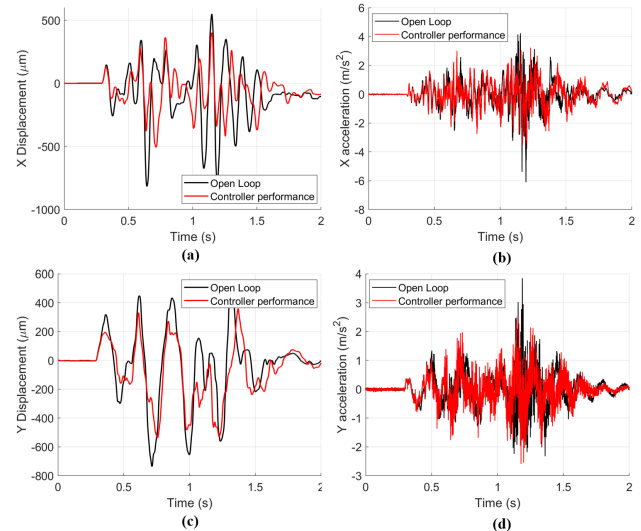

Fig. 15. All the black curves are the open loop measurements, and all the red curves are the controlled closed loop measurement. (a): the hand unit displacement in X-axis (b): the FOUP acceleration in X-axis; (c): the hand unit displacement in Y-axis (d): the FOUP acceleration in Y-axis

V. DISCUSSION

The designed multi-axis DOBCs successfully suppressed the OHT hand unit vibration displacement in multiple axes

simultaneously. Reduction in vibration peaks of the FOUP acceleration is also verified with an on-board sensor. The disturbance observer played a major role in eliminating the main disturbance dynamics, and the parallel PI controller handled the coupled dynamics inherent to our testbed design. As mentioned earlier, this effect is negligible in the real system.

With the multi-axis DOBCs concept verified, the control performance can be improved by using a larger counterbalancing VCA with a longer traveling range and larger maximum force. This allows better suppression of large acceleration peaks and avoids the impact of the VCA as it reaches its range limit. The current control VCA (VCAR0033-0224-00A; SUPT Motion) has a maximum output force $F_{max} = 33$ N and maximum stroke $2x = 22.4$ mm. The zero position is set to the middle of the stroke, thus the maximum distance the moving mass can travel in one direction is $x = 11.2$ mm. The moving mass (the magnet) is 1 kg. The maximum momentum the control VCA can offer before the moving mass collides with the base is $P_{max} = Ft = F\sqrt{2x/\alpha} = F\sqrt{2xm/F} = \sqrt{2xmF} = 0.86$ Ns. Take the multi-axis Open loop FOUP X-axis acceleration into consideration. The maximum acceleration happens near 1.2 sec. By integrating the acceleration at that peak, it shows that the velocity change is 0.077 m/s^2. The total mass of the moving part (hand unit and FOUP) is 12 kg, thus the momentum needed to suppress that acceleration peak is 0.924 Ns, which exceeds the maximum momentum our current actuator could offer. Moreover, if the force demand calculated from the controller is smaller than F_{max}, the momentum gained from the vibration suppression system will be even smaller. As a result, the collision between the moving mass and the base would occur if the gains of the second PI controller are small.

After upgrading the vibrations suppression system with a more powerful actuator, the same control system design methodology can be used with some parameter tuning to improve the vibration suppression performance.

VI. CONCLUSION AND FUTURE WORK

In this work, an inertia-based counterbalancing system is developed for FOUP vibration control. Since no sensors are allowed on the FOUP, this work focuses on the multi-axis OHT vibration control and verifies that the OHT vibration control effectively suppresses the FOUP vibration in multiple axes. A testbed is designed to apply disturbance to the OHT hand unit in the traveling axis (X-axis) and the lateral axis (Y-axis) simultaneously. A multi-axis vibration suppression system is also designed for intertia-based counterbalancing to the hand unit in both axes simultaneously. With the designed testbed, system modeling and identification is applied to derive the numerical linear model for the inputs (F_x and F_y) and outputs (x and y). Based on the linear model, a Disturbance Observer-Based Controller is developed and implemented on the hardware in both axes. With disturbance applied in both X-axis and Y-axis, and with the DOBCs in both axes turned on simultaneously, the hand unit displacement is suppressed 38% in X-axis and 27% in Y-axis, and the FOUP acceleration is suppressed 42% in X-axis and 33% in Y-axis.

In the future, a more powerful inertia-based vibration suppression system will be developed to allow further optimization of the controller parameters. Moreover, improving the spring-damper clamp system can help to further reduce the vibration transferred from OHT hand unit displacement to the FOUP acceleration. Design of flexures with embedded piezo actuators in the new clamp is part of on-going work to further improve the vibration suppression performance.

REFERENCES

[1] Daren Dance and Karen Gildersleeve. "Estimating semiconductor yield from equipment particle measurements". In: *[1992 Proceedings] IEEE/SEMI International Semiconductor Manufacturing Science Symposium*. IEEE. 1992, pp. 18–23.

[2] Moonkyu Lee and Se-Jin Yook. "Investigation of particulate contamination of heated wafers contained in a closed environment". In: *Journal of Aerosol Science* 88 (2015), pp. 148–158.

[3] Sara Case et al. "Impact of FOUP environment on product yield in advanced technologies". In: *2016 27th Annual SEMI Advanced Semiconductor Manufacturing Conference (ASMC)*. IEEE. 2016, pp. 168–171.

[4] Aly Mousaad Aly. "Vibration control of high-rise buildings for wind: a robust passive and active tuned mass damper". In: *Smart Structures and Systems* 13.3 (2014), pp. 473–500.

[5] Said Elias and Vasant Matsagar. "Research developments in vibration control of structures using passive tuned mass dampers". In: *Annual Reviews in Control* 44 (2017), pp. 129–156.

[6] Haoran Zuo, Kaiming Bi, and Hong Hao. "Using multiple tuned mass dampers to control offshore wind turbine vibrations under multiple hazards". In: *Engineering Structures* 141 (2017), pp. 303–315.

[7] Fu-Cheng Wang et al. "Decoupled robust vibration control of an optical table". In: *Journal of Vibration and Control* 20.1 (2014), pp. 38–50.

[8] Peter Heiland. *Active vibration isolation system*. US Patent 8,682,609. Mar. 2014.

[9] Hirotaka Tokoro, Motohiro Kawafuku, and Makoto Iwasaki. "An application of state feedback control to actual vehicle vibration suppression". In: *2014 IEEE 13th International Workshop on Advanced Motion Control (AMC)*. IEEE. 2014, pp. 185–190.

[10] Shuyou Yu et al. "Disturbance observer based control for four wheel steering vehicles with model reference". In: *IEEE/CAA Journal of Automatica Sinica* 5.6 (2016), pp. 1121–1127.

[11] Jiajie Qiu et al. "Disturbance Rejection Control for Active Vibration Suppression of Overhead Hoist Transport Vehicles in Semiconductor Fabs". In: *Machines* 11.2 (2023), p. 125.